

Revisit of directed flow in relativistic heavy-ion collisions from a multiphase transport model

Chong-Qiang Guo,^{1,2} Chun-Jian Zhang,^{1,2} and Jun Xu^{*1}

¹*Shanghai Institute of Applied Physics, Chinese Academy of Sciences, Shanghai 201800, China*

²*University of Chinese Academy of Sciences, Beijing 100049, China*

(Dated: November 21, 2017)

We have revisited several interesting questions on how the rapidity-odd directed flow is developed in relativistic $^{197}\text{Au}+^{197}\text{Au}$ collisions at $\sqrt{s_{NN}} = 200$ and 39 GeV based on a multiphase transport model. As the partonic phase evolves with time, the slope of the parton directed flow at midrapidity region changes from negative to positive as a result of the later dynamics at 200 GeV, while it remains negative at 39 GeV due to the shorter life time of the partonic phase. The directed flow splitting for various quark species due to their different initial eccentricities is observed at 39 GeV, while the splitting is very small at 200 GeV. From a dynamical coalescence algorithm with Wigner functions, we found that the directed flow of hadrons is a result of competition between the coalescence in momentum and coordinate space as well as further modifications by the hadronic rescatterings.

PACS numbers: 25.75.-q, 25.75.Ld, 24.10.Lx

I. INTRODUCTION

The main purpose of relativistic heavy-ion collision experiments is to study the properties of the quark-gluon plasma (QGP) [1–4] and to understand the hadron-quark phase transition. The anisotropic flow, defined as $v_n = \langle \cos[n(\phi - \Psi_n)] \rangle$ with ϕ being the particle azimuthal angle in momentum space with respect to the event plane Ψ_n and $\langle \dots \rangle$ denoting the event average, is an important observable in characterizing how the anisotropy in the initial coordinate space develops into that in the final momentum space, as a result of the strong interaction in the QGP matter created in relativistic heavy-ion collisions. The first-order anisotropic flow is named as the directed flow (v_1) (see Ref. [5] for a recent review), and it contains the rapidity-odd component and the rapidity-even component. The rapidity-odd component $v_1^{odd}(y) = -v_1^{odd}(-y)$, which is traditionally called the sideward flow, is attributed to the collective sideways deflection of particles. The rapidity-even component $v_1^{even}(y) = v_1^{even}(-y)$ was realized recently [6, 7], and it is attributed to the event-by-event fluctuation in the initial state of the colliding nuclei. In the present study we only talk about the rapidity-odd component of the directed flow.

Recently, RHIC-STAR Collaboration have reported the directed flow of protons and pions in the beam-energy-scan program [8]. It has been found that the slope of the net-proton directed flow changes sign twice between $\sqrt{s_{NN}} = 11.5$ GeV and 39 GeV, and has a minimum between $\sqrt{s_{NN}} = 11.5$ GeV and 19.6 GeV. Besides, splittings of the directed flow between protons and antiprotons as well as that between π^+ and π^- were observed at lower collision energies but become small at

higher collision energies. Efforts have been made in understanding the above directed flow data [9–14]. In this study we investigate several interesting topics relevant to the directed flow in relativistic heavy-ion collisions within a multiphase transport (AMPT) model [15]. Different from the previous study [16], we have studied the non-monotonic evolution of the directed flow in the partonic phase, the splitting of the directed flow between different quark species, and the effects of the hadronization and hadronic evolution on the directed flow. The study helps clarify how the directed flow is developed or modified at different stages in relativistic heavy-ion collisions, and is useful in understanding the directed flows at different collision energies. The rest of the paper is organized as follows. Section II provides a brief introduction of the AMPT model. The detailed analysis and discussions of the directed flow results are given in Sec. III. Finally, a summary and outlook is given in Sec. IV.

II. THE AMPT MODEL

The string melting version of the AMPT model [15], which is used in the present study, mainly consists of four parts: the initial condition generated by Heavy Ion Jet Interaction Generator (HIJING) model [17], the partonic evolution described by Zhang’s parton cascade (ZPC) model [18], a coalescence model to describe the hadronization process, and the hadronic evolution described by a relativistic transport (ART) model [19]. The HIJING model generates hadrons with proton-proton scatterings as the building brick together with the nuclear shadowing effect and the Glauber geometry for the colliding nuclei at relativistic energies. The initial phase-space distribution of partons is generated by melting hadrons produced by elastic and inelastic scatterings of participant nucleons in HIJING. The partonic interaction in the ZPC model is described by the partonic two-body elastic

*Corresponding author: xujun@sinap.ac.cn

scatterings with the differential cross section given by

$$\frac{d\sigma}{dt} \approx \frac{9\pi\alpha_s^2}{2(t - \mu^2)^2}, \quad (1)$$

where t is the standard Mandelstam variable for four-momentum transfer. In the present study we set the strong coupling constant α_s to be 0.47 and the parton screening mass μ to be 3.2264 fm^{-1} , leading to the total cross section of 3 mb. Partons freeze out continuously after their last scatterings, and the hadronization is treated according to the freeze-out phase-space distribution of all partons. The hadronization in AMPT is described by a spatial coalescence model which allows a pair of nearest quark and antiquark to form a meson and three nearest quarks (antiquarks) to form a baryon (antibaryon), with the mass and species of the hadron determined by the invariant mass and the flavors of these constituent partons. In the present study we do the coalescence for baryons and antibaryons before that for mesons. In this way there are more combinations of quarks (antiquarks) close in phase space to form baryons (antibaryons), which helps to give a smooth v_1 , while meson v_1 is not much affected since there are still plenty of choices for daughter quarks/antiquarks to form mesons. In order to see the effect of a more realistic coalescence on the directed flow, we have also checked with the dynamical coalescence [20] based on the Wigner function calculation detailed in Sec. IIIB and APPENDIX A. The spatial coalescence in the AMPT model is followed by the ART model that contains various elastic, inelastic, and decay channels to describe the hadronic evolution.

III. ANALYSIS AND RESULTS

In the present study, we employ the AMPT model to investigate the directed flow in midcentral ($b = 5 \text{ fm}$) $^{197}\text{Au} + ^{197}\text{Au}$ collisions at $\sqrt{s_{NN}} = 200$ and 39 GeV, corresponding to the top RHIC energy and a typical energy in the beam-energy-scan program. Typically, we focus on the time evolution of v_1 , the splitting of v_1 for various particle species, and the hadronization effect on v_1 . The directed flow is calculated from $v_1 = \langle \cos(\phi - \Psi_{RP}) \rangle$ with respect to the theoretical reaction plane $\Psi_{RP} = 0$.

A. Time evolution of v_1 in the partonic phase

The directed flows of partons in midcentral Au+Au collisions at $\sqrt{s_{NN}} = 200$ GeV and 39 GeV at different time steps are displayed in Fig. 1, where the upper (lower) panels show the evolutions in early (later) stages, with the solid lines from a cubic fit of $v_1(y) = F_1 y + F_3 y^3$. The initial v_1 at both collision energies are very small as expected. It is seen that the slope of the directed flow at $\sqrt{s_{NN}} = 200$ GeV grows to a maximum negative value in early stages ($t < 4 \text{ fm/c}$), and then gradually becomes

positive in later stages, while that at $\sqrt{s_{NN}} = 39$ GeV grows to a maximum negative value and becomes saturated. The maximum slope is larger at 39 GeV than at 200 GeV. By monitoring the density evolution, we found that the strong scatterings among partons mostly end around $4 \sim 6 \text{ fm/c}$. However, it is seen that the later dynamics reverses the slope of the directed flow at $\sqrt{s_{NN}} = 200$ GeV but is unable to reverse that at $\sqrt{s_{NN}} = 39$ GeV, due to the shorter life time of the partonic phase at lower collision energies. The non-monotonic behavior of the directed flow was also observed in Refs. [9, 21]. The feature mentioned above is qualitatively consistent with the less negative v_1 slope at midrapidities at higher collision energies observed by PHOBOS [22] and STAR [8, 23] Collaborations.

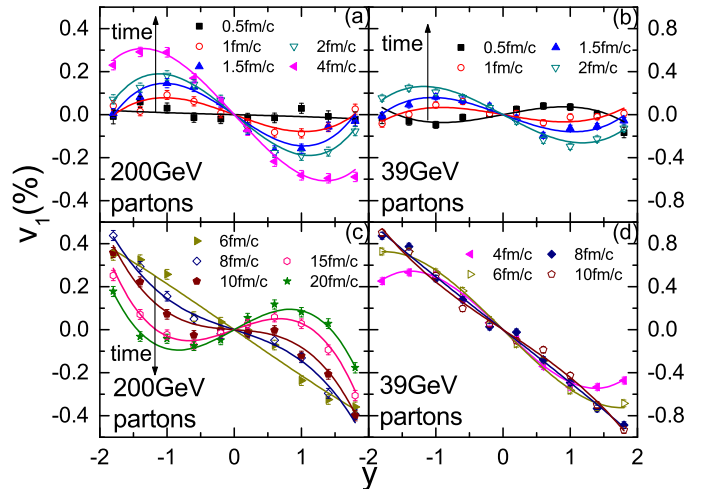


FIG. 1: (Color online) Directed flow (v_1) of partons versus rapidity (y) at different time steps in midcentral Au+Au collisions at $\sqrt{s_{NN}} = 200$ GeV (left) and 39 GeV (right). The upper panels show the behavior in early stages, while the lower panels show that in later stages.

The time evolution of the directed flow slope at midrapidities is displayed in the upper panels of Fig. 2. It is clearly seen that at $\sqrt{s_{NN}} = 200$ GeV the directed flow slope first drops to a negative value lower than -0.3% and then increases to a positive value of about 0.15% . At $\sqrt{s_{NN}} = 39$ GeV, however, the directed flow slope drops to about -0.6% and the later dynamics only slightly modifies the slope. We have further displayed the integrated directed flow at forward and backward rapidities as a function of time in the lower panels of Fig. 2. It is interesting to see that the integrated v_1 at the forward (backward) rapidity monotonically becomes more negative (positive) as the system evolves, although the directed flow at different rapidity regions changes in a complicated manner as shown in Fig. 1. At $\sqrt{s_{NN}} = 200$ GeV the integrated directed flow becomes saturated at about 8 fm/c , while at $\sqrt{s_{NN}} = 39$ GeV it is saturated at a later time. In addition, the magnitude of the integrated v_1 is larger at lower collision energies.

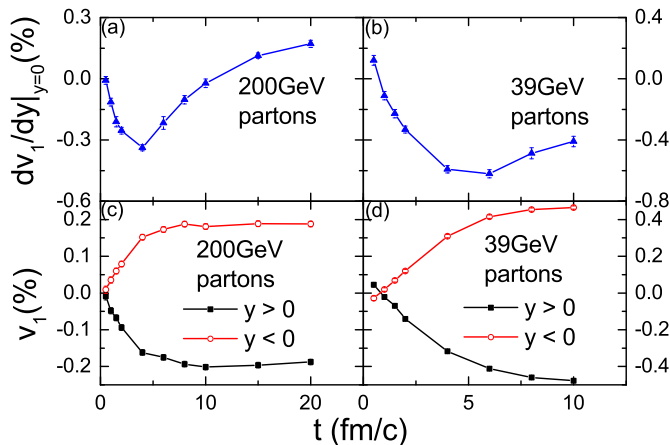


FIG. 2: (Color online) Time evolution of the parton directed flow slope ($dv_1/dy|_{y=0}$) (upper panels), and the integrated directed flow (v_1) at forward and backward rapidities (lower panels) in midcentral Au+Au collisions at $\sqrt{s_{NN}} = 200$ GeV [(a) and (c)] and 39 GeV [(b) and (d)].

We have further investigated the time evolution of the v_1 slope given the saturated integrated directed flow at both forward and backward rapidities as shown in Fig. 2. We found that the time evolution of v_1 is due to the transfer of particles, which contribute positively or negatively to v_1 , among different rapidity regions. At the later stage of the partonic phase at $\sqrt{s_{NN}} = 200$ GeV, more particles that contribute to the positive flow stay in the midrapidity region, while those contribute to the negative flow move to larger rapidities. At $\sqrt{s_{NN}} = 39$ GeV, the saturation of v_1 takes longer time while the life time of the partonic phase is too short to reverse v_1 , leading to a negative slope at the freeze-out stage.

B. Splitting of v_1 for various quark species

The results discussed in the previous subsection are averaged over all quark species. On the other hand, it is always observed that there are splittings of quantities between particles and their antiparticles as well as those between particles of different isospin states, especially at lower collision energies. The typical examples are splittings of the elliptic flow [24] and the directed flow [8] between protons and antiprotons as well as those between π^+ and π^- .

Figure 3 displays the directed flow of u and d quarks as well as their antiquarks at their freeze-out stage in midcentral Au+Au collisions at $\sqrt{s_{NN}} = 200$ GeV and 39 GeV. At $\sqrt{s_{NN}} = 200$ GeV the v_1 splitting between quarks and antiquarks as well as that between u and d quarks are already seen but the difference is comparable to the statistical error, while at $\sqrt{s_{NN}} = 39$ GeV it is clearly seen that antiquarks have a more negative directed flow slope than quarks. We note that here quarks include produced and transported ones from ini-

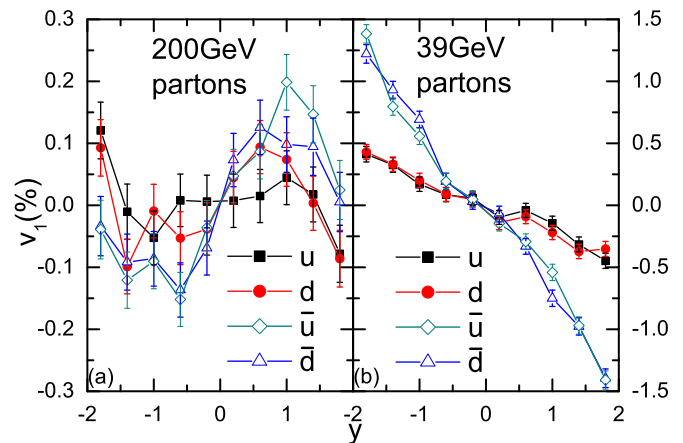


FIG. 3: (Color online) Final directed flow (v_1) of u , d , \bar{u} , and \bar{d} quarks versus rapidity (y) in midcentral Au+Au collisions at $\sqrt{s_{NN}} = 200$ GeV (a) and 39 GeV (b).

tial inelastic and elastic scatterings of participant nucleons, respectively, while antiquarks are all produced from inelastic nucleon-nucleon scatterings. As shown in Refs. [25, 26], produced and transported particles generally have different collective flows. The splitting between directed flows of various quark species could be partially responsible for the v_1 splitting between protons and antiprotons as well as that between π^+ and π^- , as reported in Ref. [8].

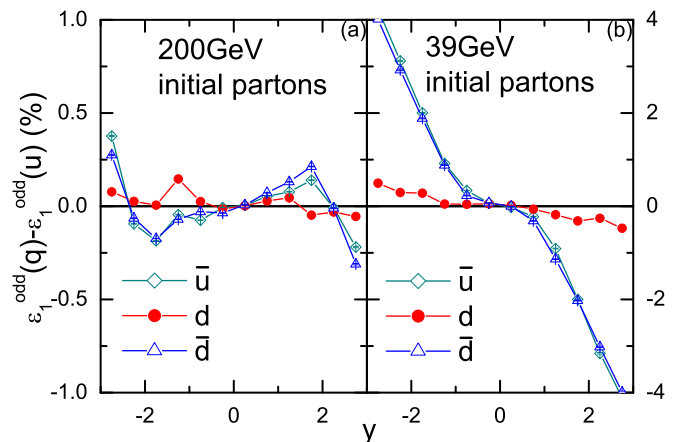


FIG. 4: (Color online) Initial first-order eccentricity ϵ_1^{odd} of d , \bar{u} , and \bar{d} quarks with respect to that of u quarks versus rapidity y in midcentral Au+Au collisions at $\sqrt{s_{NN}} = 200$ GeV (a) and 39 GeV (b).

Since the dynamics in the partonic phase dominated by the parton scattering cross section [Eq. (1)] is independent of the quark species, the splitting of the directed flows of various quark species shown in Fig. 3 can only be due to their different initial eccentricities. The mechanism how the initial eccentricity (ϵ_n) develops into the final elliptic flow (v_2) and triangular flow (v_3) has been extensively studied (see, e.g., Refs. [27–29]). The response

of the rapidity-even directed flow to the rapidity-even ϵ_1^{even} was discussed in Refs. [6, 7]. The initial rapidity-odd ϵ_1^{odd} according to the particle azimuthal angle ϕ_s in coordinate space can be calculated as [21, 30]

$$\epsilon_1^{odd}(y) = \langle \cos(\phi_s - \Psi_{RP}^{pp}) \rangle_y, \quad (2)$$

with $\langle \dots \rangle_y$ denoting the event average at a given rapidity y , and we used the theoretical reaction plane ($\Psi_{RP}^{pp} = 0$) consistent with the calculation of the rapidity-odd directed flow. Figure 4 shows the rapidity distribution of $\epsilon_1^{odd}(y)$ of d , \bar{u} , and \bar{d} quarks with respect to that of u quarks at both $\sqrt{s_{NN}} = 200$ GeV and 39 GeV. It is seen that at $\sqrt{s_{NN}} = 200$ GeV the initial ϵ_1^{odd} has small difference especially between quarks and antiquarks, while at $\sqrt{s_{NN}} = 39$ GeV the difference in the slope with respect to rapidity for different quark species is much larger. Since these partons are melted from hadrons produced in HIJING, the difference is attributed to the different production mechanisms of hadrons that have different baryon or isospin charges. The different v_1 of d , \bar{u} , and \bar{d} quarks compared with that of u quarks is attributed to their different ϵ_1^{odd} at $\sqrt{s_{NN}} = 39$ GeV. In addition, we found the initial averaged ϵ_1^{odd} is slightly larger at lower collision energies, responsible for the larger saturated v_1 observed in Fig. 2.

C. Effect of hadronization on v_1

The directed flow of freeze-out partons discussed in the previous subsections will be modified in the hadronization process. In the present study we investigate the hadronization from a dynamical coalescence model [20, 31] and the default spatial coalescence model as in AMPT. In the dynamical coalescence model, partons that are close in phase space have a larger probability to form hadrons, while in the default spatial coalescence model in AMPT, hadrons are formed by nearest combinations of partons in coordinate space as discussed in Sec. II, and all partons are forced to be used up after hadronization.

In the dynamical coalescence model, the probability to form a hadron is proportional to the parton Wigner function of that hadron, and the proportional coefficient is the statistical factor by considering the spin, flavor, and color degeneracies. For detailed formulae we refer the reader to APPENDIX A. There are also other hadronization mechanisms, such as the fragmentation of high-momentum partons in transport models and the Cooper-Frye hadronization in hydrodynamic models. However, the dynamical coalescence has already included the main feature of quark recombination, which explains the number of constituent quark scaling of collective flows [20, 32] as one of the evidences of the formation of QGP. To speed up the calculation, we skip the parton combinations with large relative momenta, since their probabilities to form hadrons are small.

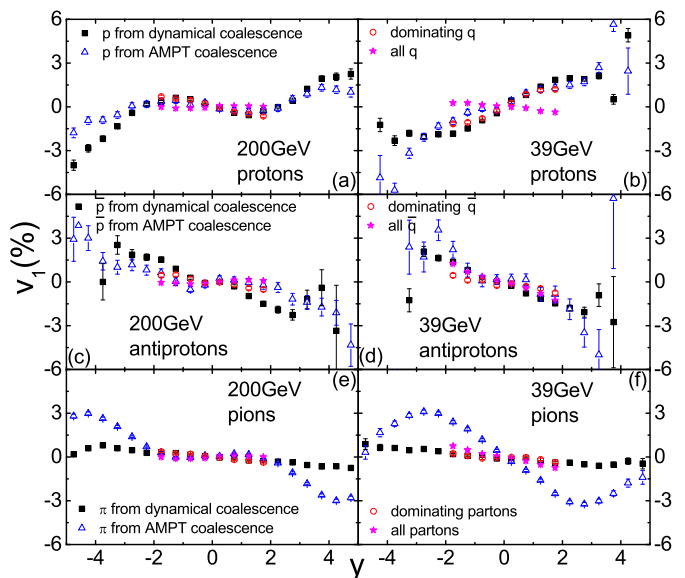


FIG. 5: (Color online) Directed flows (v_1) of protons (top), antiprotons (middle), and charged pions (bottom) from the dynamical coalescence (squares) and from the default spatial coalescence in the AMPT model (triangles), as well as v_1 of their dominating constituent quarks or antiquarks weighted by the Wigner function (circles), and v_1 of all quarks or antiquarks at their freeze-out stage as a function of rapidity in midcentral Au+Au collisions at $\sqrt{s_{NN}} = 200$ GeV (left) and 39 GeV (right). See text for details.

Figure 5 displays the directed flows of protons (top panels), antiprotons (middle panels), and charged pions (bottom panels) from the dynamical coalescence and from the default spatial coalescence in AMPT, as well as that of their dominating constituent quarks or antiquarks weighted by the Wigner function, and that of all quarks or antiquarks at their freeze-out stage. The difference between v_1 from the dynamical coalescence and that from the default spatial coalescence in AMPT is observed, consistent with the statement in Ref. [9] that the directed flow is sensitive to the hadronization treatment. It is interesting to see that the directed flow of constituent quarks (antiquarks) weighted by the Wigner function is quite different from that of all quarks (antiquarks) at their freeze-out stage. This means that in the dynamical coalescence scenario only part of partons close in phase space dominate the contribution of forming hadrons, while their directed flow is quite different from the rest partons. On the other hand, the directed flow slope of formed protons, antiprotons, or pions is different from that of their constituent partons or the overall partons. The difference is larger for baryons or antibaryons than for mesons. It is seen that the v_1 slope of protons from the dynamical coalescence changes its sign compared with that of the overall quarks.

In order to understand how the coalescence modifies the directed flow, we employ the pure momentum coalescence and pure coordinate coalescence, by consid-

ering only the momentum or the coordinate part in Eqs. (A.3) and (A.7). This is similar to the limit of choosing an infinitely large or a zero Gaussian width for the Wigner function, respectively. With the pure momentum coalescence, we found that the slope sign of v_1 near the midrapidity region is not changed after coalescence, comparing with the parton directed flow at freeze-out, consistent with the picture of the naive coalescence scenario [32, 33], which leads to the number of constituent quark scaling relation, i.e., $V_1(\mathbf{p}) \approx 2v_1(\mathbf{p}/2)$ for mesons and $\tilde{V}_1(\mathbf{p}) \approx 3v_1(\mathbf{p}/3)$ for baryons as detailed in APPENDIX B. With the pure coordinate coalescence, the parton density distribution becomes important, and the slope sign of v_1 is generally changed. The hadron directed flow is a result of competition between the coalescence in momentum and coordinate space, with the weight determined by the Gaussian width fitted by the root-mean-square radius of the hadron.

Here we further illustrate why the pure coordinate coalescence generally changes the slope sign of the directed flow. Figure 6 displays the distribution of the parton freeze-out time. In the dynamical coalescence scenario partons that freeze out at a similar time are more likely to coalesce with each other. We found that the early freeze-out partons, i.e., those freeze out before $t_{fz} = 5$ fm/c at 200 GeV and $t_{fz} = 4$ fm/c at 39 GeV, dominate the hadron formation, and their freeze-out times are indicated by the shadow. After propagating these early freeze-out partons to $t = 5$ fm/c at 200 GeV and $t = 4$ fm/c at 39 GeV, the density contour in the reaction plane (x - z) plane is shown in Fig. 7. We found that partons at $x \cdot z > 0$ ($x \cdot z < 0$) contribute positively (negatively) to the directed flow. Although there are more partons at $x \cdot z > 0$ ($x \cdot z < 0$) for 200 GeV (39 GeV), which leads to the net positive (negative) directed flow slope near midrapidity, the local density is slightly higher at $x \cdot z < 0$ ($x \cdot z > 0$) for 200 GeV (39 GeV), leading to the change of the v_1 slope sign from a pure coordinate coalescence, especially for baryons formed by three quarks close in coordinate space.

D. Effect of hadronic evolution on v_1

The directed flow of hadrons after hadronization presented in the previous subsection is further modified by the hadronic evolution described by ART, containing various elastic, inelastic, and decay channels. To illustrate the effect of hadronic rescatterings on v_1 in the AMPT model, we present in Fig. 8 the directed flow of initial (before ART) and final (after ART) protons (top panels), antiprotons (middle panels), and charged pions (bottom panels) in midcentral Au+Au collisions at $\sqrt{s_{NN}} = 200$ GeV and 39 GeV. After hadronic rescatterings, it is seen that the slope of the directed flow generally becomes less negative or increases, while the sign of the v_1 slope near midrapidity region is mostly not changed. The effect of the hadronic evolution on v_1 is seen to be larger at lower

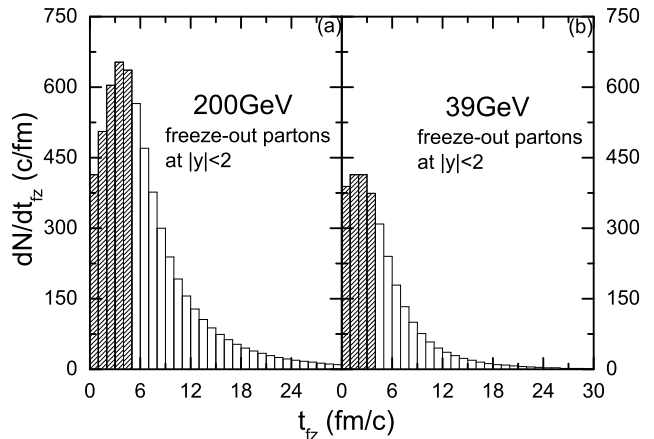


FIG. 6: Distribution of parton freeze-out time in midcentral Au + Au collisions at $\sqrt{s_{NN}} = 200$ GeV (a) and $\sqrt{s_{NN}} = 39$ GeV (b), with the shadow indicating the early freeze-out partons that dominate the hadron formation.

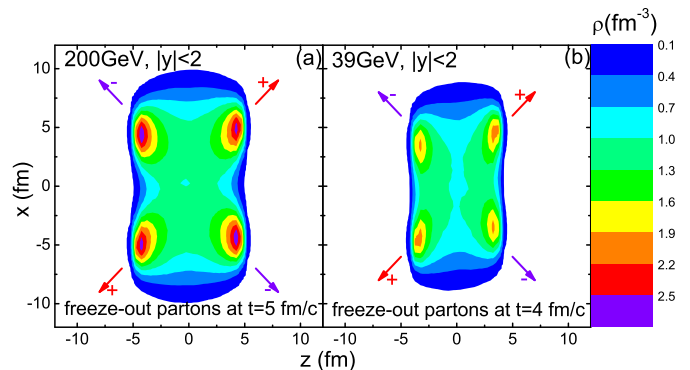


FIG. 7: (Color online) Density contours of freeze-out partons in the midrapidity region in the x - z plane in midcentral Au + Au collisions at $t = 5$ fm/c for $\sqrt{s_{NN}} = 200$ GeV (a) and at $t = 4$ fm/c for $\sqrt{s_{NN}} = 39$ GeV (b), with different colors indicating the parton number densities. The particles that move in the “+(-)” direction contribute to the positive flow (antiflow).

collision energies compared to that at higher collision energies.

IV. SUMMARY AND OUTLOOK

Based on the framework of a multiphase transport model, we have discussed some interesting topics relevant to how the directed flow is developed in relativistic heavy-ion collisions, which have not been well addressed previously. As the partonic phase evolves, a non-monotonic behavior of the directed flow is observed at higher collision energies, and the later dynamics is able to change the slope sign of the directed flow at midrapidity region, due to the transfer of partons among dif-

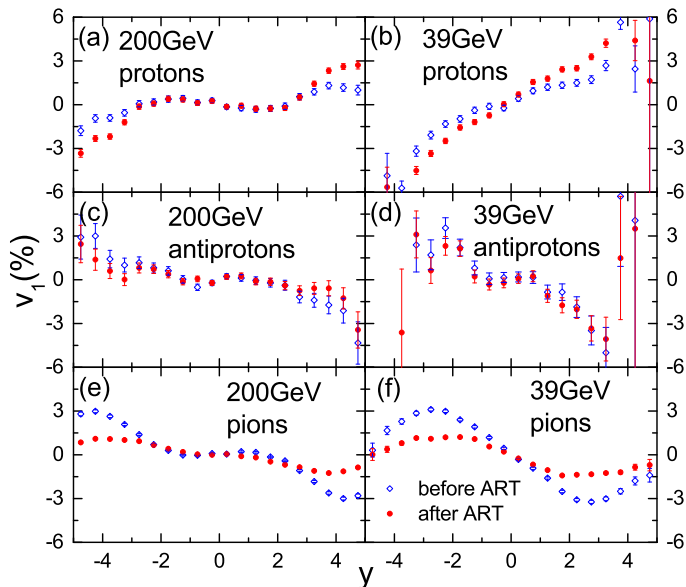


FIG. 8: (Color online) Directed flow (v_1) of protons (top), antiprotons (middle), and charged pions (bottom) versus rapidity (y) before and after hadronic rescatterings in midcentral Au+Au collisions at $\sqrt{s_{NN}} = 200$ GeV (left) and 39 GeV (right).

ferent rapidity regions, but this is not observed at lower collision energies as a result of shorter life time of the partonic phase. The splitting of the directed flow for various quark species is observed at lower collision energies due to their different initial rapidity-odd eccentricities, while such splitting becomes very small at higher collision energies. The directed flow of hadrons is a result of competition between the coalescence in momentum and coordinate space, with the weight determined by the Gaussian width of the Wigner function in the dynamical coalescence scenario, and is further modified by the hadronic rescatterings. The coalescence mechanism as well as the hadronic rescatterings discussed in the present manuscript can be possible reasons accounting for the violation of the number of constituent quark scaling for the directed flow mentioned in Ref. [34].

In the future study, we will improve the coalescence and introduce the mean-field potentials, or similarly, the equation of state [35–38], to the multiphase transport model as in Refs. [39, 40]. It will be of great interest to study quantitatively how the results obtained in this work are modified by the mean-field potentials, which are expected to be different for different quark and hadron species. Based on the studies of the directed flow from particle scatterings in the present study as well as the mean-field potentials in the future study, one should be able have a better understanding of the directed flow at various collision energies and for various particle species, thus hopefully extract useful information of the hadron-quark phase transition and the QCD phase diagram.

Acknowledgments

We thank Chen Zhong for maintaining the high-quality performance of the computer facility. This work was supported by the Major State Basic Research Development Program (973 Program) of China under Contract Nos. 2015CB856904 and 2014CB845401, the National Natural Science Foundation of China under Grant Nos. 11475243 and 11421505, the “100-talent plan” of Shanghai Institute of Applied Physics under Grant Nos. Y290061011 and Y526011011 from the Chinese Academy of Sciences, and the Shanghai Key Laboratory of Particle Physics and Cosmology under Grant No. 15DZ2272100.

APPENDIX A. DYNAMICAL COALESCENCE FOR HADRONS WITH WIGNER FUNCTION

In the dynamical coalescence model, the probability for a pair of quark and antiquark to form a meson is proportional to the quark Wigner function of the meson times the statistical factor, i.e.,

$$f_M(\boldsymbol{\rho}, \mathbf{k}_\rho) = 8g_M \exp\left(-\frac{\boldsymbol{\rho}^2}{\sigma_\rho^2} - \mathbf{k}_\rho^2 \sigma_\rho^2\right), \quad (\text{A.3})$$

where $g_M = 1/36$ is the statistical factor for pions, and

$$\boldsymbol{\rho} = \frac{1}{\sqrt{2}}(\mathbf{r}_1 - \mathbf{r}_2), \quad (\text{A.4})$$

$$\mathbf{k}_\rho = \sqrt{2} \frac{m_2 \mathbf{k}_1 - m_1 \mathbf{k}_2}{m_1 + m_2} \quad (\text{A.5})$$

are the relative distance in the coordinate and momentum space for the two-particle system, with m_i , \mathbf{r}_i , and \mathbf{k}_i being the mass, coordinate, and momentum of the i th particle, respectively. The width parameter σ_ρ is related to the root-mean-square (RMS) radius of the meson through the relation

$$\begin{aligned} \langle r_M^2 \rangle &= \frac{3}{2} \frac{m_1^2 + m_2^2}{(m_1 + m_2)^2} \sigma_\rho^2 \\ &= \frac{3}{4} \frac{m_1^2 + m_2^2}{m_1 m_2 (m_1 + m_2) \omega}, \end{aligned} \quad (\text{A.6})$$

where the second line follows if we use the relation $\sigma_\rho = 1/\sqrt{\mu_1 \omega}$ in terms of the oscillator frequency ω and the reduced mass $\mu_1 = 2(1/m_1 + 1/m_2)^{-1}$.

Similarly, the probability for three light quarks to form a baryon is expressed as

$$\begin{aligned} f_B(\boldsymbol{\rho}, \boldsymbol{\lambda}, \mathbf{k}_\rho, \mathbf{k}_\lambda) \\ = 8^2 g_B \exp\left(-\frac{\boldsymbol{\rho}^2}{\sigma_\rho^2} - \frac{\boldsymbol{\lambda}^2}{\sigma_\lambda^2} - \mathbf{k}_\rho^2 \sigma_\rho^2 - \mathbf{k}_\lambda^2 \sigma_\lambda^2\right), \end{aligned} \quad (\text{A.7})$$

where $g_B = 1/108$ is the statistical factor for protons,

and

$$\boldsymbol{\lambda} = \sqrt{\frac{2}{3}} \left(\frac{m_1 \mathbf{r}_1 + m_2 \mathbf{r}_2}{m_1 + m_2} - \mathbf{r}_3 \right), \quad (\text{A.8})$$

$$\mathbf{k}_\lambda = \sqrt{\frac{3}{2}} \frac{m_3 (\mathbf{k}_1 + \mathbf{k}_2) - (m_1 + m_2) \mathbf{k}_3}{m_1 + m_2 + m_3} \quad (\text{A.9})$$

are the relative distance in the coordinate and momentum space between the third particle and the system formed by the first and the second particles. The width parameter σ_λ is related to the oscillator frequency via $1/\sqrt{\mu_2 \omega}$, with $\mu_2 = (3/2)[1/(m_1 + m_2) + 1/m_3]^{-1}$. The RMS radius of the baryon is then given by

$$\langle r_B^2 \rangle = \frac{1}{2} \frac{m_1^2(m_2 + m_3) + m_2^2(m_1 + m_3) + m_3^2(m_1 + m_2)}{(m_1 + m_2 + m_3)m_1 m_2 m_3 \omega}. \quad (\text{A.10})$$

The RMS radius of the produced hadron is taken from Ref. [41], which is 0.61 fm for π^+ and 0.877 fm for protons, respectively.

APPENDIX B. NAIVE COALESCENCE SCENARIO

In the naive coalescence scenario, the momentum distribution of quarks inside hadrons is neglected. A meson with momentum \mathbf{p} are formed by a pair of quark and antiquark with half the meson momentum $\mathbf{p}/2$ co-moving in the same direction. This is actually the limit of the dynamical coalescence with $\omega = 0$ or infinitely large Gaussian width in the Wigner function. In the following, we briefly remind the relation between collective flows of hadrons and their constituent quarks in the naive coalescence scenario as in Refs. [32, 33].

The azimuthal distribution of mesons in momentum space can be expressed as

$$F(\phi, \mathbf{p}) \propto 1 + 2 \sum_{n=1}^{\infty} V_n(\mathbf{p}) \cos(n\phi) \propto f(\phi, \mathbf{p}/2)^2, \quad (\text{B.11})$$

where $f(\phi)$ is azimuthal distribution function of partons, i.e.,

$$f(\phi, \mathbf{p}/2) \propto 1 + 2 \sum_{n=1}^{\infty} v_n(\mathbf{p}/2) \cos(n\phi). \quad (\text{B.12})$$

From Eqs. (B.11) and (B.12), the n th-order anisotropy flow $V_n(\mathbf{p})$ of mesons can be expressed in terms of the

parton anisotropy flow $v_n(\mathbf{p}/2)$ as

$$V_n = \frac{1}{N} (2v_n + \sum_{i=1}^{n-1} v_i v_{n-i} + 2 \sum_{i=1}^{\infty} v_i v_{n+i}), \quad (\text{B.13})$$

with $N = 1 + 2 \sum_{i=1}^{\infty} v_i^2$.

Similarly, the azimuthal distribution for baryons in momentum space can be expressed as the third power of the azimuthal distribution for partons, i.e.,

$$\tilde{F}(\phi, \mathbf{p}) \propto 1 + 2 \sum_{n=1}^{\infty} \tilde{V}_n(\mathbf{p}) \cos(n\phi) \propto f(\phi, \mathbf{p}/3)^3 \quad (\text{B.14})$$

The n th-order anisotropy flow \tilde{V}_n of baryons is expressed in terms of the parton anisotropy flow $v_n(\mathbf{p}/3)$ as

$$\begin{aligned} \tilde{V}_n = & \frac{1}{\tilde{N}} (3v_n + 3 \sum_{i=1}^{n-1} v_i v_{n-i} + 6 \sum_{i=1}^{\infty} v_i v_{n+i} \\ & + 3 \sum_{i=1}^{\infty} \sum_{j=1}^{\infty} v_i v_j v_{n+i+j} + 3 \sum_{i=1}^{\infty} \sum_{j=1}^{n+i-1} v_i v_j v_{n+i-j} \\ & + \sum_{i=1}^{n-1} \sum_{j=1}^{n-i-1} v_i v_j v_{n-(i+j)}), \end{aligned} \quad (\text{B.15})$$

with $\tilde{N} = 1 + 6 \sum_{i=1}^{\infty} v_i^2 + 6 \sum_{i=1}^{\infty} \sum_{j=1}^{\infty} v_i v_j v_{i+j}$.

Neglecting the higher-order terms, the scaling relations between the directed flows of baryons (\tilde{V}_1), mesons (V_1), and partons (v_1) are

$$V_1(\mathbf{p}) \approx \frac{2v_1(\mathbf{p}/2)}{1 + 2v_1^2(\mathbf{p}/2)} \approx 2v_1(\mathbf{p}/2), \quad (\text{B.16})$$

$$\tilde{V}_1(\mathbf{p}) \approx \frac{3v_1(\mathbf{p}/3)}{1 + 6v_1^2(\mathbf{p}/3)} \approx 3v_1(\mathbf{p}/3). \quad (\text{B.17})$$

Note that the scaling relation for the rapidity-even directed flow or the higher-order anisotropic flows ($n > 2$) is often discussed at midrapidities ($y \approx 0$), where the momentum \mathbf{p} can be approximated by the transverse momentum p_T . In the most general case, the momentum \mathbf{p} is a vector related to both the rapidity y and the transverse momentum p_T , as in the present study of the rapidity-odd directed flow.

-
- [1] I. Arsene *et al.* (PHOBOS Collaboration), Nucl. Phys. **A757**, 1 (2005).
 [2] B. B. Back *et al.* (BRAHMS Collaboration), Nucl. Phys. **A757**, 28 (2005).

- [3] J. Adams *et al.* (STAR Collaboration), Nucl. Phys. **A757**, 102 (2005).
 [4] K. Adcox *et al.* (PHENIX Collaboration), Nucl. Phys. **A757**, 184 (2005).

- [5] S. Singha *et al.*, *Advances in High Energy Physics* **16**, 2836989 (2016).
- [6] D. Teaney and L. Yan, *Phys. Rev. C* **83**, 064904 (2011).
- [7] M. Luzum and J. Y. Ollitrault, *Phys. Rev. Lett.* **106**, 102301 (2011).
- [8] L. Adamczyk *et al.* (STAR Collaboration), *Phys. Rev. Lett.* **112**, 162301 (2014).
- [9] J. Steinheimer *et al.*, *Phys. Rev. C* **89**, 054913 (2014).
- [10] V. P. Konchakovski *et al.*, *Phys. Rev. C* **90**, 014903 (2014).
- [11] Y. Nara *et al.*, *Phys. Rev. C* **94**, 034906 (2016).
- [12] Y. Nara, H. Niemi, J. Steinheimer, and H. Stöcker, *Phys. Lett. B* **769**, 543 (2017).
- [13] Yu. B. Ivanov and A. A. Soldatov, *Phys. Rev. C* **91**, 024915 (2015).
- [14] P. Batyuk, D. Blaschke, M. Bleicher, Yu. B. Ivanov, Iu. Karpenko, S. Merts, M. Nahrgang, H. Petersen, and O. Rogachevsky, *Phys. Rev. C* **94**, 044917 (2016).
- [15] Z. W. Lin, C. M. Ko, B. A. Li, B. Zhang, and S. Pal, *Phys. Rev. C* **72**, 064901 (2005).
- [16] J. Y. Chen, J. X. Zuo, X. Z. Cai, F. Liu, Y. G. Ma, and A. H. Tang, *Phys. Rev. C* **81**, 014904 (2010).
- [17] X. N. Wang and M. Gyulassy, *Phys. Rev. D* **44**, 3501 (1991).
- [18] B. Zhang, *Comput. Phys. Commun.* **109**, 193 (1998).
- [19] B. A. Li and C. M. Ko, *Phys. Rev. C* **52**, 2037 (1995).
- [20] V. Greco, C. M. Ko, and P. Levai, *Phys. Rev. Lett.* **90**, 202302 (2003); *Phys. Rev. C* **68**, 034904 (2003).
- [21] H. Liu, S. Panitkin, and N. Xu, *Phys. Rev. C* **59**, 348 (1999).
- [22] B. B. Back *et al.* (PHOBOS Collaboration), *Phys. Rev. Lett.* **97**, 012301 (2006).
- [23] B. I. Abelev *et al.* (STAR Collaboration), *Phys. Rev. Lett.* **101**, 252301 (2008).
- [24] L. Adamczyk *et al.* (STAR Collaboration), *Phys. Rev. Lett.* **110**, 142301 (2013).
- [25] J. C. Dunlop, M. A. Lisa, and P. Sorensen, *Phys. Rev. C* **84**, 044914 (2011).
- [26] Y. Guo, F. Liu, and A. H. Tang, *Phys. Rev. C* **86**, 044901 (2012).
- [27] B. Alver and G. Roland, *Phys. Rev. C* **81**, 054905 (2010).
- [28] R. A. Lacey *et al.*, *Phys. Rev. C* **83**, 044902 (2011).
- [29] H. Petersen, G. Y. Qin, S. A. Bass, and B. Müller, *Phys. Rev. C* **82**, 041901(R) (2010).
- [30] R. J. M. Snellings, H. Sorge, S. A. Voloshin, F. Q. Wang, and N. Xu, *Phys. Rev. Lett.* **84**, 2803 (2000).
- [31] C. M. Ko, T. Song, F. Li, V. Greco, and S. Plumari, *Nucl. Phys. A* **928**, 234 (2014).
- [32] P. F. Kolb *et al.*, *Phys. Rev. C* **69**, 051901(R) (2004).
- [33] J. Y. Jia and C. Zhang, *Phys. Rev. C* **75**, 031901(R) (2007).
- [34] L. Adamczyk *et al.*, [STAR Collaboration], arXiv: 1708.07132 [hep-ex].
- [35] H. Stöcker, *Nucl. Phys. A* **750**, 121 (2005).
- [36] S. A. Bass *et al.*, *Prog. Part. Nucl. Phys.* **41**, 255 (1998).
- [37] J. Brachmann *et al.*, *Phys. Rev. C* **61**, 024909 (2000).
- [38] L. P. Csernai and D. Röhrich, *Phys. Lett. B* **458**, 454 (1999).
- [39] J. Xu, T. Song, C. M. Ko, and F. Li, *Phys. Rev. Lett.* **112**, 012301 (2014).
- [40] J. Xu and C. M. Ko, *Phys. Rev. C* **94**, 054909 (2016).
- [41] J. Beringer *et al.* [Particle Data Group Collaboration], *Phys. Rev. D* **86**, 010001 (2012).